Journal of Power Sources 218 (2012) 313–319

Contents lists available at SciVerse ScienceDirect

Journal of Power Sources

journal homepage: www.elsevier.com/locate/jpowsour

$LaCoO_3$: Promising cathode material for protonic ceramic fuel cells based on a $BaCe_{0.2}Zr_{0.7}Y_{0.1}O_{3-\delta}$ electrolyte

Sandrine Ricote [a,*], Nikolaos Bonanos [a], Filip Lenrick [b], Reine Wallenberg [b]

[a] Department of Energy Conversion and Storage, Technical University of Denmark, Frederiksborgvej 399, DK-4000 Roskilde, Denmark
[b] nCHREM/Center for Analysis and Synthesis, Lund University, Box 124, SE-221 00 Lund, Sweden

HIGHLIGHTS

- Successful infiltration of $LaCoO_3$ into a porous BCY27 after 6 infiltrations of 1 mol L^{-1} solution.
- Single phased $LaCoO_3$ formed after 2 h at 600 °C in air.
- $LaCoO_3$ does not degrade nor react with BCZY27 at temperatures up to 600 °C.
- Cathode ASR of 0.39 and 0.11 Ω cm^2 in air, $pH_2O = 0.01$ atm, at 500 and 600 °C respectively.
- Oxide ion conduction is not necessary in PCFC cathodes.

ARTICLE INFO

Article history:
Received 23 April 2012
Received in revised form
18 June 2012
Accepted 29 June 2012
Available online 7 July 2012

Keywords:
PCFC
BCZY
Lanthanum cobaltite
Cathode material
Infiltration

ABSTRACT

Symmetric cells (cathode/electrolyte/cathode) were prepared using $BaCe_{0.2}Zr_{0.7}Y_{0.1}O_{3-\delta}$ (BCZY27) as proton conducting electrolyte and $LaCoO_3$ (LC) infiltrated into a porous BCZY27 backbone as cathode. Single phased LC was formed after annealing in air at 600 °C for 2 h. Scanning electron micrographs showed the presence of the infiltrated LC in the full cathode depth. Transmission electron micrographs revealed LC grains (60–80 nm) covering partly the BCZY27 grains (200 nm–1 μm). Impedance spectra were recorded at 500 °C and 600 °C, varying the oxygen partial pressure and the water vapour pressure. Two arcs correspond to the cathode contribution: a middle range frequency one (charge transfer) and a low frequency one (oxygen dissociation/adsorption). The area specific resistances (ASRs) of both contributions increase when decreasing the oxygen partial pressure. The low frequency arc is independent on the water vapour pressure while the charge transfer ASR values increase with higher pH_2O. The cathode ASRs of 0.39 and 0.11 Ω cm^2 at 500 and 600 °C respectively, in air ($pH_2O = 0.01$ atm) are the lowest reported to the authors' knowledge for PCFC cathodes. Furthermore, this work shows that the presence of oxide ion conduction in the cathode material is not necessary for good performance.

1. Introduction

After more than two decades of research on the electrolyte materials for protonic ceramic fuel cells (PCFCs) [1–4] efforts are now focused on cathode development. Additional challenges compared to those of SOFCs include formation of water vapour at the cathode side and slower electrode kinetics due to the lower operating temperatures (400–600 °C). Because of the formation of water at the cathode of PCFCs, protonic conduction in the cathode is necessary in order to extend the reaction sites to the entire gas/cathode interface. If protonic conduction is absent, the water will be formed only at the electrolyte/cathode interface. Cercer made of the electrolyte material ($BaZr_{0.1}Ce_{0.7}Y_{0.2}O_{3-\delta}$) and a mixed oxide ion and electron conductor MIEC ($Sm_{0.5}Sr_{0.5}CoO_{3-\delta}$ referred to as SSC or $Ba_{0.5}Sr_{0.5}Co_{0.8}Fe_{0.2}O_{3-\delta}$ referred to as BSCF) were used to impart protonic conduction to the cathode [5,6]. An optimal percentage of MIEC and proton conductor oxide exists for composite cathodes to get the lowest polarization resistance. In the case of SSC–$BaCe_{0.8}Sm_{0.2}O_{3-\delta}$, this value was estimated to be circa 60 wt% of SSC [7]. However, due to the high temperature required for the cercer fabrication, cation interdiffusion was observed between the electrolyte material and MIEC. Infiltration of the MIEC into a porous backbone of proton conductor material was shown to be a good alternative, as this low temperature method prevents the cation interdiffusion [8]. Infiltration of electrode materials is commonly used for SOFC [9,10]: the particle size of the infiltrated MIEC is in

* Corresponding author. Tel.: +45 46 77 56 41; fax: +45 46 77 58 58.
E-mail addresses: sari@risoe.dtu.dk, sari@dtu.dk (S. Ricote).

0378-7753/$ – see front matter © 2012 Elsevier B.V. All rights reserved.
http://dx.doi.org/10.1016/j.jpowsour.2012.06.098

the sub-100 nm range which creates a large surface area and can improve the surface-catalytic behaviour.

The cathode mechanism of PCFCs, being more complex than that of an SOFC cathode, is still not fully understood. First, Uchida et al. [11] proposed the elementary steps of a PCFC cathode by considering the addition of the formation and evolution of water to the dissociative adsorption and diffusion of oxygen species. Later on, He et al. [12] further developed these steps based on the transfer and reaction of protons. For each of these steps (i), the cathode polarization resistance (Rp) depends on the water vapour and/or the oxygen partial pressures and can be written as follow:

$$Rp_i \propto (pO_2)^{-m_i} \cdot (pH_2O)^{-n_i} \quad (1)$$

where n_i and m_i correspond the reaction orders. The different steps and expected dependences of the polarization resistance with the water vapour and oxygen partial pressures are listed in Table 1.

As mentioned above, protonic conduction is necessary in the cathode of a PCFC, in addition to the electronic conduction. But it is not known for certain whether oxide ion conduction is mandatory, as long as the cathode material exhibits good catalytic properties for oxygen dissociation. To address this question, we have chosen to study $LaCoO_3$ as PCFC cathode material because $LaCoO_3$ does not form oxygen vacancies at temperatures below 600 °C and is therefore a pure electronic conductor in the expected operating temperature range of a PCFC [13]. Indeed, the cobalt cations are not easily reduced when six-fold coordinated. Moreover $LaCoO_3$ was shown to be stable: no phase changes were observed after 350 h stability tests at 600 °C in air as well as at 400 °C in humidified air with $pH_2O = 0.2$ atm [13]. In addition to its stability in air and wet atmosphere, $LaCoO_3$ does not react with solid solutions of barium cerate–zirconate at temperatures below 1100 °C [14]. However a secondary phase ($YBaCo_2O_{5+\delta}$) was detected by XRD after heat treatment at 1270 °C [13]. $LaCoO_3$ has also been studied as SOFC cathode material, exhibiting a very low area specific resistance: 0.079 Ω cm^2 at 600 °C [15].

In this work, the performance of infiltrated $LaCoO_3$ cathodes was studied in a symmetric cell configuration: $LaCoO_3$ infiltrated in porous BCZY27/dense BCZY27 electrolyte/$LaCoO_3$ infiltrated in porous BCZY27. Microscopy and Energy Dispersive Spectroscopy (EDS) analysis were performed on the symmetric cells after testing.

2. Experimental

2.1. Preparation of symmetric cells

Dense samples of BCZY27 ($BaCe_{0.2}Zr_{0.7}Y_{0.1}O_{3-\delta}$) were prepared by solid state reactive sintering as described in Ref. [16]. Bars (8 mm·8 mm·35 mm) were made by uniaxial pressing and were sintered in air at 1500 °C for 4 h. The resulting black coloured bars were cut into 700 μm thick square slices. The surface of these substrates was manually polished with a 500 grade SiC paper.

BCZY27 powder was prepared by conventional solid state reaction at 1400 °C for 30 h in air. A slurry was prepared using this BCZY27 powder, Solsperse 20 wt% in Terpineol, dibutylphthalat as plasticizer and 5 wt% ethylcellulose in Terpineol as binder. A layer was screen printed on each side of the dense BCZY27 substrate with a Polyester 92 mesh using a blade speed of 60 mm s^{-1}. The samples were dried at 90 °C in a rolling furnace and were then fired at 1300 °C for 2 h in air. The resulting BCZY27 porous backbone is beige/light brown. The La and Co nitrate solution (1 mol L^{-1}) was prepared in a similar way as described elsewhere [15]. A drop of solution was deposited on one side and the sample was dried at 70 °C on a heating plate, followed by the same procedure on the second side. Between each infiltration, the samples were calcined at 350 °C for 30 min in air. After the last infiltration, the calcination time at 350 °C was extended to 2 h. The samples were infiltrated 6 times on both sides and finally annealed in air at 600 °C for 2 h.

2.2. Characterization of the samples

Crystallographic phases were determined at room temperature with a Stoe X-ray diffractometer, in the $\theta/2\theta$ mode, using the K_α1Cu radiation.

Micrographs of polished and unpolished cross sections were recorded using field-emission gun scanning electron microscopes (SEM): JEOL JSM-6700F and Nova NanoLab 600 FIB/SEM. Deposition of a thin carbon layer was necessary because of the insulating properties of the samples. The porosity of the cathodes was determined from the polished cross section micrographs by estimating the area occupied by pores (low intensity) divided by the total image area. The uncertainty of this determination arises from the difficulty of fixing the intensity threshold separating pores from material. An electron transparent specimen was prepared by focus ion beam (FIB) *in-situ* lift out technique [17,18] using an FEI Nova NanoLab 600 FIB/SEM and investigated in a JEOL 3000F transmission electron microscope (TEM). Scanning transmission electron microscopy (STEM) was used to record micrographs with a high angle annular dark field (HAADF) detector and energy dispersive spectroscopy (EDS) maps using an Oxford Instruments INCA X-Max silicon drift detector. Si, which could come from the polishing, was not detected in the analyses.

For AC electrical measurements, Pt current collectors (Ferro) were painted on the samples and heated in-situ to 600 °C in air. Impedance spectra were recorded at 600 and 500 °C in five different oxygen partial pressures (mixing of air or oxygen with

Table 1
Cathode reaction steps for a PCFC cathode [11,12]. m and n are respectively the reaction orders with respect to the oxygen partial pressure and water vapour pressure.

Step	Process	Elementary reaction	m	n
1	Adsorption of oxygen gas	$O_2\,(g) \rightarrow 2\,O_{ad}$	1	0
2	Reduction of the adsorbed oxygen	$O_{ad} + e^- \rightarrow O^-_{ad}$	3/8	0
3	Diffusion of the oxygen from the surface to the TPB	$O^-_{ad} \rightarrow O^-_{TPB}$	1/4	0
4	Charge transfer of the oxygen	$O^-_{TPB} + e^- \rightarrow O^{2-}_{TPB}$	0	0
5	Diffusion of the proton from the electrolyte to the TPB	$H^+_{electrolyte} \rightarrow H^+_{TPB}$	0	1/2
6	Reaction proton/oxygen to form hydroxide at TPB	$H^+_{TPB} + O^{2-}_{TPB} \rightarrow OH^-_{TPB}$	0	1/2
7	Reaction proton/hydroxide to form water at TPB	$H^+_{TPB} + OH^-_{TPB} \rightarrow H_2O_{TPB}$	0	1
8	Desorption of water	$H_2O_{TPB} \rightarrow H_2O\,(g)$	0	1

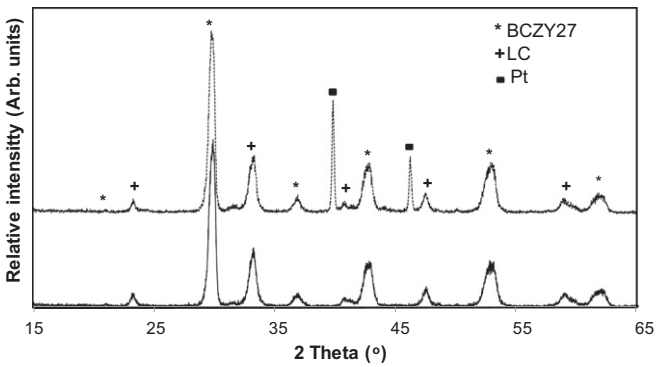

Fig. 1. XRD pattern before (solid line) and after (dotted line) electrochemical testing on the $LaCoO_3$ (LC) infiltrated cells. The diffractograms are shifted vertically for clarity.

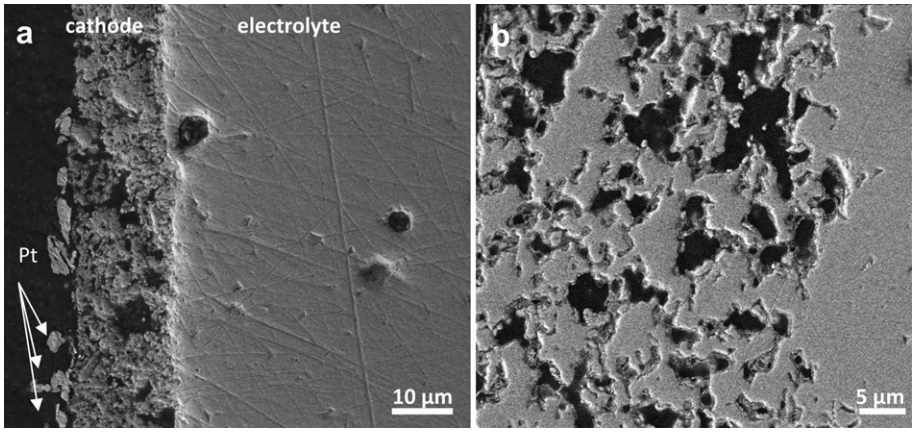

Fig. 2. Secondary electron SEM micrographs of the $LaCoO_3$ (LC) infiltrated BCZY27 cathode/BCZY27 electrolyte (polished cross sections): a) overview micrograph of the cathode–electrolyte (the Pt particles are residuals from the paste used as current collector) b) close up micrograph of the cathode.

nitrogen) and four different steam conditions (change of the temperature of the water bubbler). The spectra were recorded with a Hioki LCR analyser in the frequency range of 0.05 Hz–1 MHz, with an amplitude of 100 mV. After correction of the parasitic inductance, the spectra were analysed with *Zsimpwin* software using parallel arrangements of a resistor and constant phase element. The area specific resistances (i.e. the polarization resistance normalized to an area of 1 cm^2) presented in this work are the values averaged over 8 samples.

3. Results and discussion

Fig. 1 displays the diffractograms recorded on a cell after annealing 2 h at 600 °C (solid line) and on the same cell after the electrochemical testing (dotted line). In the later case, Pt peaks are present in addition to the BCZY27 and LC phases, corresponding to the Pt current collectors used for AC measurements. No indication of reaction between LC and BCZ27 or degradation of LC is seen.

Fig. 2a is a micrograph of a polished cross section of a tested symmetric cell. Residual Pt particles from the paste used as current collector are visible. A higher magnification micrograph (Fig. 2b) was used to estimate the porosity to 33 ± 2%. The thickness of the cathode is about 20 μm, with micron-scaled pores.

Secondary electron micrographs with higher magnification were also recorded on non-polished cross sections such as Fig. 3. The infiltrate network was observed in the full cathode depth. It is difficult to estimate the grain size of the LC infiltrate but one can easily see the bigger BCZY27 grains (200 nm–1 μm) covered partly by much smaller particles (below 100 nm). TEM images were recorded to determine the grain size of the LC infiltrate: between 60 and 80 nm. An example is shown in Fig. 4.

EDS maps of the cathode–electrolyte are displayed in Fig. 5. For clarity, only the Ce map is presented in the figure but similar maps were obtained for Ba, Zr and Y, showing that these four elements are present in both the cathode and the electrolyte. La and Co on the contrary are present only in the cathode, as expected. The quantification of the different elements, presented in Table 2 (atomic percentage), confirms these results.

Fig. 6 is an impedance spectrum recorded at 500 °C in humidified air with $pH_2O = 0.01$ atm. The spectrum was fitted using the equivalent circuit $R_1(R_2Q_2)(R_3Q_3)(R_4Q_4)$. The different impedance arcs were allocated to the corresponding processes using the

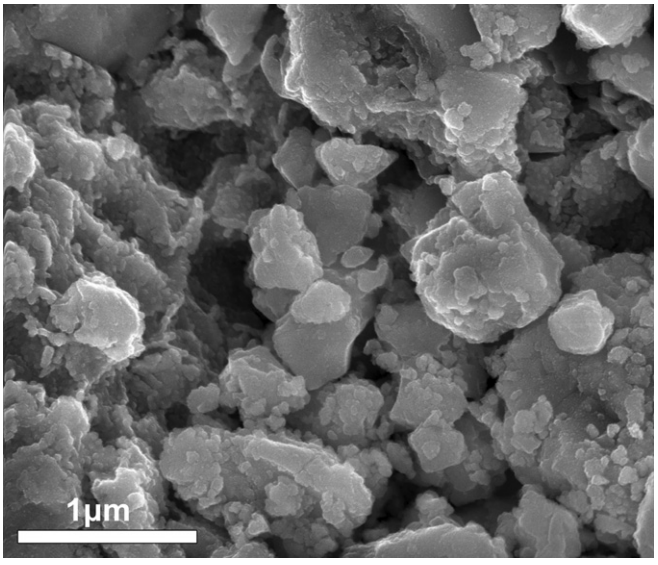

Fig. 3. Secondary electron SEM micrograph of a fractured $LaCoO_3$ (LC) infiltrated BCZY27 cathode.

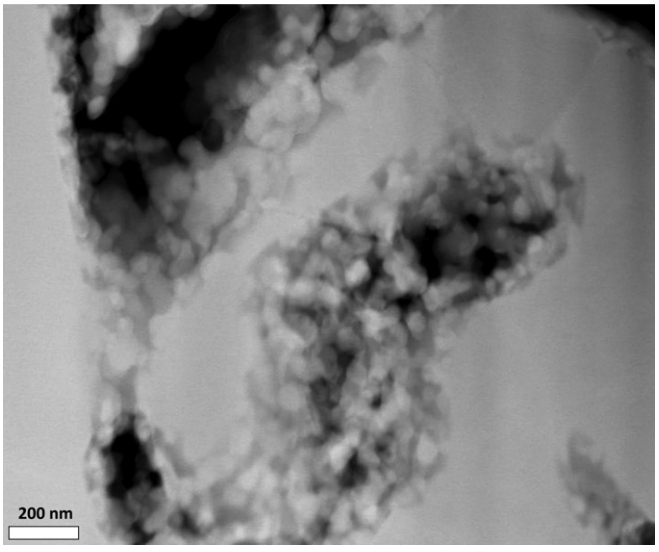

Fig. 4. STEM-HAADF micrograph of the interface between the BCZY27 electrolyte (leftmost) and the $LaCoO_3$ (LC) infiltrated BCZY27 cathode.

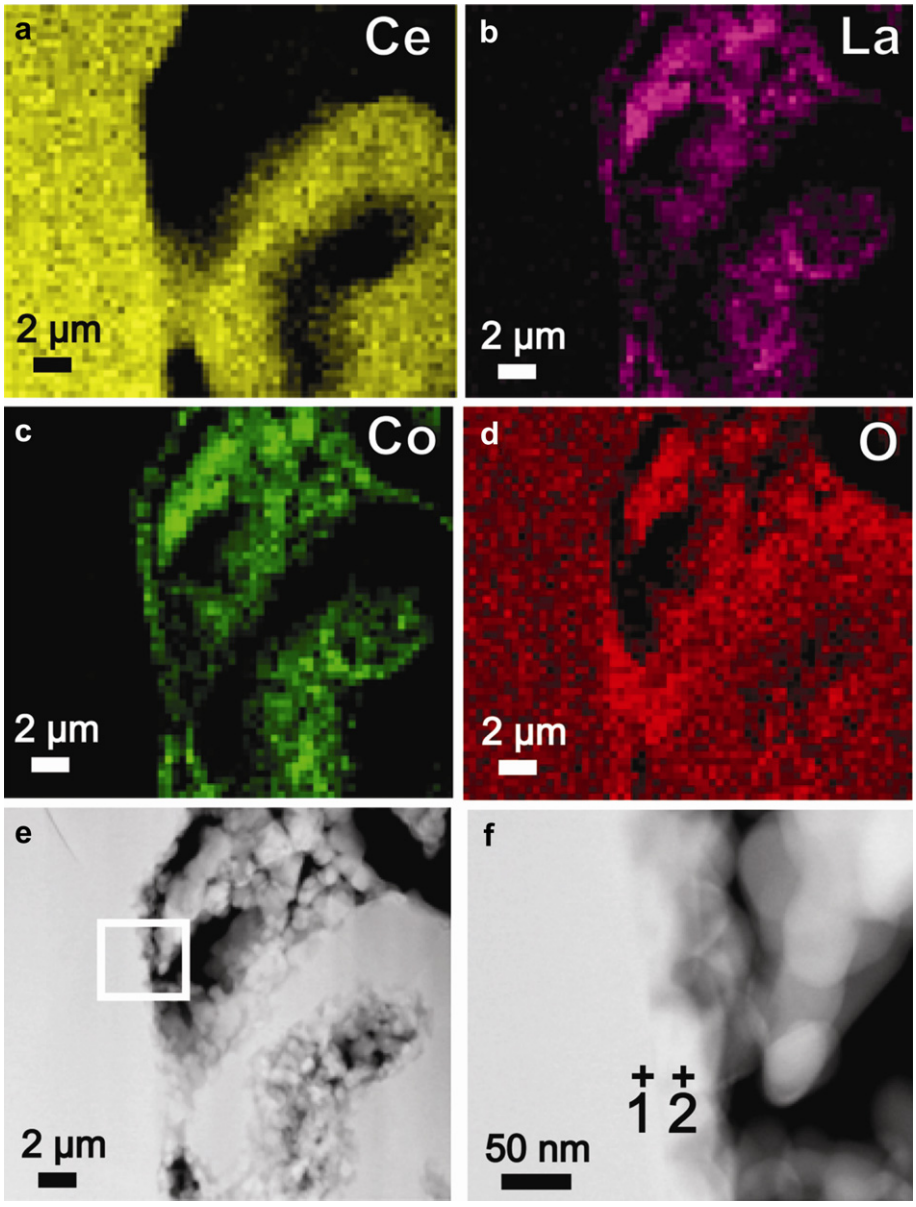

Fig. 5. a) The BCZY27 electrolyte (left) and part of the $LaCoO_3$ (LC) infiltrated BCZY27 backbone, here exemplified by the Ce La1 EDS map, b)-c) The $LaCoO_3$ infiltrate with the La La1 in (b) and Co Ka1 in (c), d) O Ka1 EDS map, e) STEM-HAADF image of the corresponding mapped area and f) STEM-HAADF image at higher magnification, area marked in e). Full quantifications at positions 1 and 2 are displayed in Table 2.

pseudo capacitance (C) related to each arc. As a result, R_1 was assigned to the bulk of the electrolyte, R_2 to the grain boundary of the electrolyte ($C_2 \sim 6 \cdot 10^{-9}$ F cm^{-2}) and R_3 and R_4 to the cathode ($C_3 \sim 1 \cdot 10^{-5}$ F cm^{-2} and $C_4 \sim 5 \cdot 10^{-1}$ F cm^{-2}). Dailly et al. [19,20] used the Schouler-type representation (i.e. plotting the relaxation frequency and the capacitance as a function of the inverse temperature) to interpret the impedance spectra recorded on

Table 2
Atomic percentage for the elements of interest quantified from point 1 (electrolyte) and point 2 (cathode) in the EDS maps of Fig. 5.

Quantification position	O	La	Co	Ba	Ce	Zr	Y	Total
1	49.2	0.0	0.7	26.0	5.2	16.8	2.1	100.00
2	51.5	17.5	17.8	8.4	0.9	4.7	−0.8	100.00

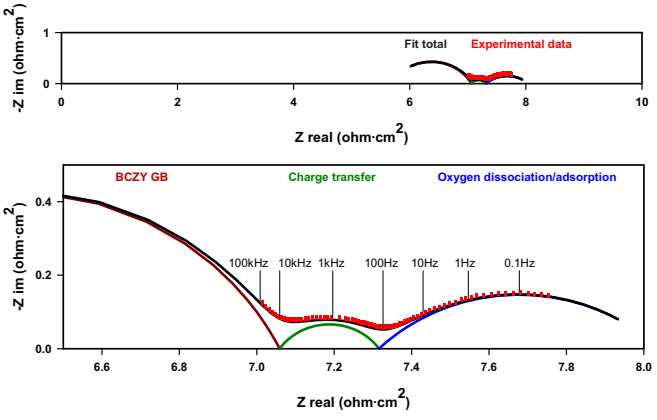

Fig. 6. Impedance spectrum at 500 °C in air, pH_2O = 0.01 atm. Dots are the experimental data and solid lines the fit using an R(RQ)(RQ)(RQ) circuit.

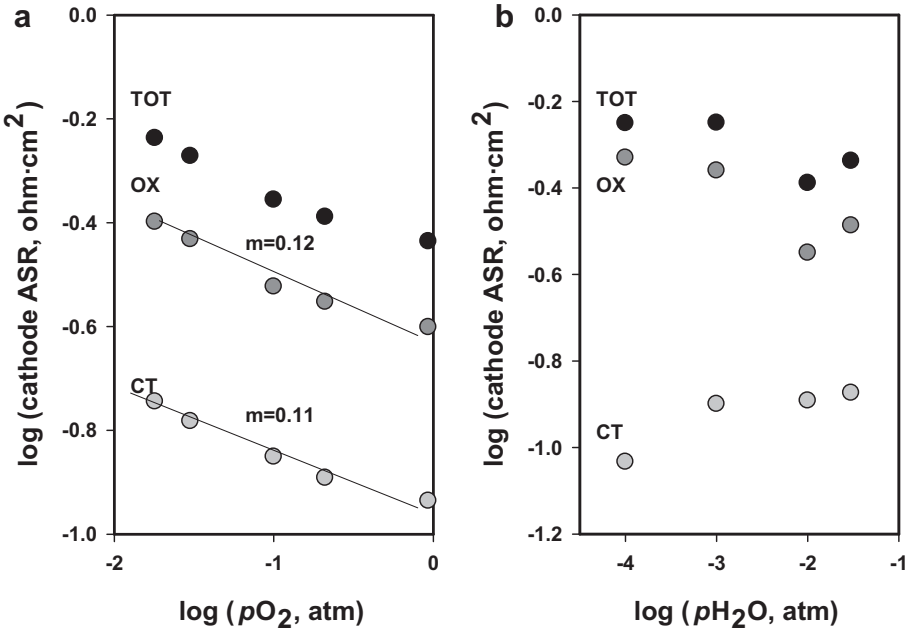

Fig. 7. ASR as a function of a) the oxygen partial pressure, $pH_2O = 0.01$ atm and b) the water vapour pressure, $pO_2 = 0.21$ atm. The abbreviations CT, OX and TOT correspond respectively to charge transfer, oxygen dissociation/adsorption and total.

several MIEC cathode materials. They concluded that the low frequency arc (i.e. R_4Q_4) is due to the oxygen adsorption/dissociation steps, overlapped with the diffusion process, and the middle-range frequency arc (R_3Q_3) is due to the ionic charge transfer at the electrode/electrolyte interface. Grimaud et al. [21] also used series of (RQ) elements for the analysis of the impedance spectra recorded on MIEC materials and assigned the two cathode arcs to the interface charge transfer (middle-range frequency) and to the electrode reaction (low frequency). He et al. [12] and Peng et al. [22] reported that the low frequency arc might correspond to the surface diffusion of adsorbed oxygen, whereas the middle-range frequency one suggested the migration of protons to the TPBs (due to the activation energy of 0.6 eV). Similarly low activation energy values for the middle-range frequency contribution were measured on an infiltrated LSCF [8].

When trying to distinguish the charge transfer and oxygen dissociation/adsorption contributions at 600 °C, the values had a high uncertainty because of the very small impedance of the cathode compared to that of the electrolyte. Indeed, a total area specific resistance (ASR) of 0.11 Ω cm^2 was estimated at 600 °C in humidified air with $pH_2O = 0.010$ atm. As a result, only the data at 500 °C were used to study the variation of each cathode contribution with the oxygen and water vapour partial pressures, as shown in Fig. 7a and b respectively. Firstly, it is noted that the ASR values of the oxygen dissociation/adsorption are 3 times larger than those of the charge transfer contribution. Secondly, the ASR values of both the oxygen dissociation/adsorption and the charge transfer increase when decreasing the oxygen partial pressure. The reaction orders are similar, 0.12 and 0.11 respectively, and do not correspond to any one of the 8 steps presented in Introduction. These results are different from those of He et al. [12] and Peng et al. [22] who found that, at 500 °C, the low frequency arc (i.e. the oxygen dissociation/adsorption) depended on the oxygen partial pressure with a reaction order of 0.24 and the middle range frequency arc did not depend on the oxygen partial pressure. The main difference is that the cathode material studied here (LC) is a pure electronic conductor (no oxide ion conduction) while Peng et al. [22] investigated a mixed oxygen ion and electron conductor.

Table 3
Electrolyte conductivity values (mS cm^{-1}) at various oxygen partial pressures, $pH_2O = 0.01$ atm at 500 and 600 °C.

Temp. (°C)	$pO_2 = 0.97$ atm	$pO_2 = 0.20$ atm	$pO_2 = 0.10$ atm	$pO_2 = 0.03$ atm	$pO_2 = 0.018$ atm
500 °C	8.6	8.2	7.9	7.6	7.3
600 °C	13.9	12.2	11.5	10.5	9.9

The charge transfer ASR of the LC infiltrated in BCZY27 increases with increasing water vapour pressure (Fig. 7b), contrary to an expected decrease (equation (1)). This trend was already observed for LSCF [8,21]. Even though this increase of the ASR could not be completely explained, it was concluded that it was linked to the absence of proton conduction in LSCF. Similarly, LC is not known to exhibit proton conduction. The ASR values of the oxygen dissociation/adsorption contribution are rather scattered, and appear not to depend on the water vapour pressure.

The electrolyte conductivity values at 500 and 600 °C at different the oxygen partial pressures are summarized in Table 3. These values are found to be 3–4 times larger than those reported for BCZY27. Indeed, values of 1.6 and 3.4 mS cm^{-1} were reported in humidified air with $pH_2O = 0.015$ atm, at 500 and 600 °C respectively [23]. This increase cannot be explained by La and Co interdiffusion (not observed by the EDS maps) nor by the formation of a second phase (none detected by XRD). Oxide ion conduction is also ruled out in the studied temperature range, as it was shown that the transport number of protons in BCZY27 is equal to 1 at 500 °C and 0.98 at 600 °C [24]. It is not known whether this conduction is generated by ions or electron-holes. Tests on full cell configuration (Ni–BCZY27 cermet/thin film of BCZY27/LC infiltrated in porous BCZY27) will clarify whether this increase of the electrolyte is beneficial or detrimental to the performances.

Finally, the ASR values of the LC infiltrated in BCZY27 are very encouraging: 0.39 and 0.11 Ω cm^2 in humidified air with $pH_2O = 0.010$ atm at 500 and 600 °C respectively. To our knowledge, they are the lowest reported so far for PCFC cathode. A

Table 4
Cathode area specific resistance (Ω cm^2) from literature in air at 600 °C (measured on symmetric cells).

Cathode material	Electrolyte	Cathode fabrication method	$p(H_2O)$ (atm)	R_p (Ω cm^2)	Ref.
$LaCoO_3$	BCZY27	Infiltration into	0.01	0.11	This work
		porous backbone	0.03	0.14	This work
$Ba_{0.5}Sr_{0.5}Co_{0.8}Fe_{0.2}O_{3-\delta}$	$BaCe_{0.9}Y_{0.1}O_{3-\delta}$	Screen printing	0.03	~1.5	[19]
		Spray deposition	–	~0.5	[25]
$La_{0.6}Sr_{0.4}Co_{0.2}Fe_{0.8}O_{3-\delta}$	$BaCe_{0.9}Y_{0.1}O_{3-\delta}$	Screen printing	0.03	~6	[19]
	$BaCe_{0.9}Y_{0.1}O_{3-\delta}$	Painting of slurry	0.03	~7.9	[26]
$La_{0.58}Sr_{0.4}Co_{0.2}Fe_{0.8}O_{3-\delta}$	BCZY27	Spray pyrolysis	0.001	0.61	[8]
			0.03	0.89	[8]
		Infiltration into	0.001	0.63	[8]
		porous backbone	0.03	0.98	[8]
		Screen printed	0.01	0.8	Internal report
$Pr_2NiO_{4+\delta}$	$BaCe_{0.9}Y_{0.1}O_{3-\delta}$	Screen printing	0.03	~1.5	[19]
$PrBaCo_2O_{5+\delta}$	$BaZr_{0.1}Ce_{0.7}Y_{0.2}O_{3-\delta}$	Spray deposition	–	0.73	[27]
$Y_{0.5}Pr_{0.5}BaCo_2O_{5+\delta}$	$BaZr_{0.1}Ce_{0.7}Y_{0.2}O_{3-\delta}$	Spray deposition	–	0.59	[27]
$Ca_3Co_4O_{9+\delta}$	$BaCe_{0.9}Y_{0.1}O_{3-\delta}$	Painting of slurry	0.03	2.2	[28]
$Ca_{2.7}La_{0.3}Co_4O_{9+\delta}$	$BaCe_{0.9}Y_{0.1}O_{3-\delta}$	Painting of slurry	0.03	~2.2	[28]
$La_{0.6}Sr_{0.4}Co_{0.2}Fe_{0.8}O_{3-\delta}/BaCe_{0.9}Yb_{0.1}O_{3-\delta}$ composite (1:1 by weight)	$BaCe_{0.8}Y_{0.2}O_{3-\delta}$	Painting of slurry	0.03	~1.1	[26]
$Pr_{0.58}Sr_{0.4}Fe_{0.8}Co_{0.2}O_{3-\delta}/BaCe_{0.9}Yb_{0.1}O_{3-\delta}$composite (60:40 by volume)	$BaCe_{0.9}Y_{0.1}O_{3-\delta}$	Screen printing	0.023	~1.2	[29]
$Pr_{0.58}Sr_{0.4}Fe_{0.8}Co_{0.2}O_{3-\delta}/BaCe_{0.9}Yb_{0.1}O_{3-\delta}$ composite (50:50 by volume)	$BaCe_{0.9}Y_{0.1}O_{3-\delta}$	Screen printing	0.023	~1.25	[29]
$Pr_{0.58}Sr_{0.4}Fe_{0.8}Co_{0.2}O_{3-\delta}/BaCe_{0.9}Yb_{0.1}O_{3-\delta}$ composite (40:60 by volume)	$BaCe_{0.9}Y_{0.1}O_{3-\delta}$	Screen printing	0.023	~1.4	[29]
$Sm_{0.5}Sr_{0.5}CoO_{3-\delta}$ (SSC)	$BaCe_{0.8}Sm_{0.2}O_{3-\delta}$	Infiltration of SSC in $BaCe_{0.8}Sm_{0.2}O_{3-\delta}$	–	0.21	[30]
$Sm_{0.5}Sr_{0.5}CoO_{3-\delta}/BaCe_{0.8}Sm_{0.2}O_{3-\delta}$ composite (55:45 by weight)	$BaCe_{0.8}Sm_{0.2}O_{3-\delta}$	Screen printing	–	0.67	[30]
LSCF/$BaZr_{0.5}Pr_{0.3}Y_{0.2}O_{3-\delta}$ composite	$BaZr_{0.5}Pr_{0.3}Y_{0.2}O_{3-\delta}$	Painting of slurry	0.03	0.157	[31]
LSCF/$BaZr_{0.7}Pr_{0.1}Y_{0.2}O_{3-\delta}$ composite	$BaZr_{0.7}Pr_{0.1}Y_{0.2}O_{3-\delta}$	Painting of slurry	0.03	~0.8	[31]

summary of PCFC cathode ASR measured in air in a symmetric cell configuration at 600 °C is presented in Table 4.

Whereas all the cathode materials in literature are either mixed oxide ion and electron conductor (MIEC) or composite of a proton conducting oxide and a MIEC, we showed that low cathode area specific resistances could be achieved with the infiltration of an electronic conductor ($LaCoO_3$) into a proton conducting oxide (BCZY27). Therefore, the oxide ion conduction does not seem to be necessary in a cathode for PCFC, as long as the electronic conductor has good catalytic properties for oxygen dissociation [15] and there is a large amount of triple phase boundaries such as the adsorbed oxygen has only a short distance to diffuse along the surface to the TPB where the water formation reaction takes place.

4. Conclusions

$LaCoO_3$ (LC) was successfully infiltrated into a porous backbone of BCZY27. Single phased LC was formed after 2 h in air at 600 °C. The size of the LC grains was estimated between 60 and 80 nm. Percolation of the LC infiltrate through the whole cathode was achieved with 6 infiltrations of a 1 mol L^{-1} solution. The infiltration is a promising low temperature method for cathode preparation as cation interdiffusion can be avoided: EDS maps showed the presence of La and Co only in the cathode depth. Two cathode contributions are present on the AC spectra: the charge transfer (middle range frequency) and the oxygen dissociation/adsorption (low frequency); the latter being circa 3 times larger than the former. We found that the area specific resistance (ASR) of both contributions increases with decreasing the oxygen partial pressure. The oxygen dissociation/adsorption contribution is independent on the water vapour pressure, while the ASR values of the charge transfer increase with increasing pH_2O. This phenomenon has already been observed for LSCF. The ASR values of the LC infiltrated cathode are very encouraging: 0.39 and 0.11 Ω cm^2 at 500 and 600 °C respectively in humidified air with $pH_2O = 0.010$ atm. This study also showed that oxide ion conduction in a cathode of a PCFC is not necessary to get good performances. Full cell made of Ni–BCZY27 cermet/thin film of BCZY27/LC infiltrated in porous BCZY27 will be tested.

Acknowledgements

This work was carried out within the nextgenFCmat project (*Next generation fuel cell materials*), financed by The Danish Council for Strategic Research (DSF case number 09-075900) and the Swedish Energy Agency (N-INNER D. nr 2010-000530 project nr. 32939-1). The authors would also like to thank Martin Søgaard and Alfred Junio Samson from DTU and Einar Vøllestad and Vasileios Besikiotis from University of Oslo for useful discussions, as well as Per Martin Rørvik from SINTEF for proof-reading.

References

[1] H. Iwahara, T. Esada, H. Uchida, N. Maeda, Solid State Ionics 3–4 (1981) 359.
[2] K.D. Kreuer, Annu. Rev. Mater. Res. 33 (2003) 333–359.
[3] L. Malavasi, C.A.J. Fischer, M.S. Islam, Chem. Soc. Rev. 39 (2010) 4370–4387.
[4] E. Fabbri, D. Pergolesi, E. Traversa, Chem. Soc. Rev. 39 (2010) 4366–4369.
[5] L. Yang, C. Zuo, S. Wang, Z. Cheng, M. Liu, Adv. Mater. 20 (17) (2008) 3280–3283.
[6] B. Lin, H. Ding, Y. Dong, S. Wang, X. Zhang, D. Fang, G. Meng, J. Power Sources 186 (2009) 58–61.
[7] V. Dusastre, J.A. Kilner, Solid State Ionics 126 (1999) 163–174.
[8] S. Ricote, N. Bonanos, P.M. Rørvik, C. Haavik, J. Power Sources 209 (2012) 172–179.
[9] J. Chen, F. Liang, L. Liu, S. Jiang, B. Chi, J. Pu, J. Li, J. Power Sources 183 (2008) 586–589.
[10] X. Lou, Z. Liu, S. Wang, Y. Xiu, C.P. Wong, M. Liu, J. Power Sources 195 (2010) 419–424.
[11] H. Uchida, S. Tanaka, H. Iwahara, J. Appl. Electrochem. 15 (1985) 93–97.
[12] F. He, T. Wu, R. Peng, C. Xia, J. Power Sources 194 (2009) 263–268.
[13] G. Goupil, T. Delahaye, G. Gauthier, B. Sala, F. Lefebvre-Joud, Solid State Ionics 209–210 (2012) 36–42.
[14] J.R. Tolchard, T. Grande, Solid State Ionics 178 (2007) 593–599.
[15] A.J. Samson, M. Søgaard, N. Bonanos, Electrochem. Solid State Lett. 15 (4) (2012) B1–B3.
[16] S. Ricote, N. Bonanos, A. Manerbino, W.G. Coors, Int. J. Hydrogen Energy 37 (2012) 7954–7961.
[17] M.H.F. Overwijk, F.C. van den Heuvel, C.W.T. Bulle-Lieuwma, J. Vac. Sci. Technol. B 11 (1993) 2021–2024.
[18] T. Ohnishi, H. Koike, T. Ishitan, S. Tomimatsu, K. Umemura, T. Kamino, 25th International Symposium for Testing and Failure Analysis, Santa Clara, CA, USA, 1999, pp. 449–453.
[19] J. Dailly, S. Fourcade, A. Largeteau, F. Mauvy, J.C. Grenier, M. Marrony, Electrochim. Acta 55 (2010) 5847–5853.
[20] J. Dailly, F. Mauvy, M. Marrony, M. Pouchard, J.C. Grenier, J. Solid State Electrochem. 15 (2011) 245–251.

[21] A. Grimaud, F. Mauvy, J.M. Bassat, S. Fourcade, L. Rocheron, M. Marrony, J.C. Grenier, J. Electrochem. Soc. 159 (6) (2012) B683–B694.
[22] R. Peng, T. Wu, W. Liu, G. Meng, J. Mater. Chem. 20 (2010) 6218–6225.
[23] S. Ricote, N. Bonanos, G. Caboche, Solid State Ionics 180 (2009) 990–997.
[24] S. Ricote, N. Bonanos, H.J. Wang, R. Haugsrud, Solid State Ionics 185 (2011) 1–17.
[25] Y. Lin, R. Ran, Y. Zheng, Z. Shao, W. Jin, N. Xu, J. Ahn, J. Power Sources 180 (2008) 15–22.
[26] E. Fabbri, S. Licoccia, E. Traversa, E.D. Wachsman, Fuel Cells 2 (2009) 128–138.
[27] Y. Lin, R. Ran, C. Zhang, R. Cai, Z. Shao, J. Phys. Chem. A. 114 (2010) 3764–3772.
[28] H.B. Yahia, F. Mauvy, J.C. Grenier, J. Solid State Chem. 183 (2010) 527–531.
[29] V.B. Vert, C. Solís, J.M. Serra, Fuel Cells 1 (2011) 81–90.
[30] T. Wu, Y. Zhao, R. Peng, C. Xia, Electrochim. Acta 54 (2009) 4888–4892.
[31] E. Fabbri, L. Bi, D. Pergolesi, E. Traversa, Energy Environ. Sci. 4 (2011) 4984–4993.